Dynamics of wrinkle growth and coarsening in stressed thin films

Rui Huang and Se Hyuk Im
Department of Aerospace Engineering & Engineering Mechanics, University of Texas, Austin, Texas 78712, USA
(Received 27 March 2006; published 30 August 2006)

A stressed thin film on a soft substrate can develop complex wrinkle patterns. The onset of wrinkling and initial growth is well described by a linear perturbation analysis, and the equilibrium wrinkles can be analyzed using an energy approach. In between, the wrinkle pattern undergoes a coarsening process with a peculiar dynamics. By using a proper scaling and two-dimensional numerical simulations, this paper develops a quantitative understanding of the wrinkling dynamics from initial growth through coarsening till equilibrium. It is found that, during the initial growth, a stress-dependent wavelength is selected and the wrinkle amplitude grows exponentially over time. During coarsening, both the wrinkle wavelength and amplitude increases, following a power-law scaling under uniaxial compression. More complicated dynamics is predicted under equibiaxial stresses, which starts with a faster coarsening rate before asymptotically approaching the same scaling under uniaxial stresses. At equilibrium, a parallel stripe pattern is obtained under uniaxial stresses and a chaotic labyrinth pattern under equibiaxial stresses. Under stresses of the same magnitude, the two patterns have the same average wavelength, but different amplitudes. It is noted that the dynamics of wrinkling, while analogous to other phase ordering phenomena, is distinct and rich under the effects of stress and substrate elasticity.

DOI: 10.1103/PhysRevE.74.026214 PACS number(s): 05.45.−a, 46.32.+x, 68.55.−a, 02.70.Hm

I. INTRODUCTION

Complex wrinkle patterns have been observed in various thin film systems [1–9], typically with integrated hard and soft materials for various technological applications as well as in nature. The underlying mechanism of wrinkling has been generally understood as a stress-driven instability, conceptually similar to the classical Euler buckling of a compressed column. Much of the existing theoretical work on wrinkling is based on a linear perturbation analysis [10], which determines the onset of the mechanical instability. Some recent studies [11–13] have investigated the nonlinear aspects due to large deflection, and predicted different wrinkle patterns based on the principle of energy minimization. However, the energy approach cannot address the question as to how these patterns emerge and evolve from one type to another. Recently, a spectrum of evolving wrinkle patterns has been observed in metal-polymer bilayer [14,15], exhibiting a peculiar dynamics of evolution process, which has not been well understood.

In a previous work [16], the kinetics of wrinkle growth in a stressed elastic film on a viscoelastic substrate was studied by a linear perturbation analysis, based on which a classification of wrinkling behavior was established. Subsequently, one-dimensional numerical simulations [17] revealed three stages of wrinkle evolution: initial growth, coarsening, and equilibration, in qualitative agreement with experimental observations [14,15]. While the initial growth is well described by the linear perturbation analysis and the equilibration can be analyzed using the energy approach, the dynamics of coarsening has not been quantitatively understood. By using a proper scaling and two-dimensional numerical simulations, this paper develops a quantitative understanding of the wrinkling dynamics for all three stages. The paper is organized as follows. Section II briefly outlines the mathematical model developed in the previous study [17]. In Sec. III, a scaling analysis is performed to predict the dynamics at each stage. Section IV describes a spectral method for two-dimensional numerical simulations, with the results discussed in Sec. V for both uniaxially and biaxially stressed films.

II. MODEL DESCRIPTION

A model was developed previously [17] for evolving wrinkles in a bilayer thin film consisting of an elastic layer and a viscoelastic layer as sketched in Fig. 1. The deforma-

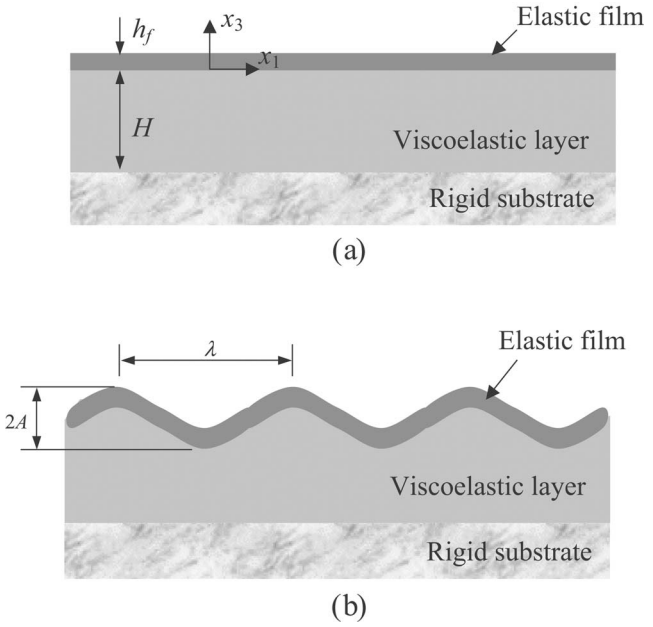

FIG. 1. Schematic of an elastic film on a viscoelastic layer supported by a rigid substrate: (a) the reference state, and (b) a wrinkled state.

tion of the elastic film is described by the von Karman plate theory [18], which gives a nonlinear relationship between the displacement and the surface traction. For the viscoelastic layer, a relationship between the surface velocity and the traction was obtained under the assumption of the Kelvin model of linear viscoelasticity and a thin-layer approximation. Coupling of the two layers through the interface leads to a set of nonlinear evolution equations:

$$\frac{\partial w}{\partial t} = \frac{1-2\nu}{2(1-\nu)}\frac{Hh_f}{\eta}\left[-\frac{\mu_f h_f^2}{6(1-\nu_f)}\nabla^2\nabla^2 w + \nabla\cdot(\boldsymbol{\sigma}\cdot\nabla w)\right] - \frac{\mu_R}{\eta}w, \tag{1}$$

$$\frac{\partial \mathbf{u}}{\partial t} = \frac{Hh_f}{\eta}\nabla\cdot\boldsymbol{\sigma} - \frac{\mu_R}{\eta}\mathbf{u}, \tag{2}$$

where $w=w(x_1,x_2,t)$ is the lateral deflection of the film and $\mathbf{u}=u_1(x_1,x_2,t)\mathbf{e}_1+u_2(x_1,x_2,t)\mathbf{e}_2$ is the in-plane displacement. The components of the in-plane stress $\boldsymbol{\sigma}$ are given by

$$\sigma_{\alpha\beta} = \sigma_{\alpha\beta}^{(0)} + 2\mu_f\left[\varepsilon_{\alpha\beta} + \frac{\nu_f}{1-\nu_f}\varepsilon_{\gamma\gamma}\delta_{\alpha\beta}\right], \tag{3}$$

where $\sigma_{\alpha\beta}^{(0)}$ is the initial residual stress in the film before wrinkling, and the in-plane membrane strain components are

$$\varepsilon_{\alpha\beta} = \frac{1}{2}\left(\frac{\partial u_\alpha}{\partial x_\beta} + \frac{\partial u_\beta}{\partial x_\alpha}\right) + \frac{1}{2}\frac{\partial w}{\partial x_\alpha}\frac{\partial w}{\partial x_\beta}. \tag{4}$$

The Greek subscripts, α, β, and γ, take on the values of the in-plane coordinates, 1 and 2, and a repeated subscript implies summation over 1 and 2. In addition to the initial stress, the physical parameters for the elastic film include h_f for the thickness, μ_f for the shear modulus, and ν_f for Poisson's ratio. Similarly, for the viscoelastic layer, we have H for the thickness, η for the viscosity, μ_R for the rubbery modulus, and ν for Poisson's ratio.

While both the lateral deflection and the in-plane displacement are involved during wrinkling, the main characteristics of the evolution dynamics can be drawn from Eq. (1) for the lateral deflection. By regrouping the physical parameters, Eq. (1) can be rewritten in a mathematically simpler form

$$\frac{\partial w}{\partial t} = -K\nabla^2\nabla^2 w + F\nabla\cdot(\boldsymbol{\sigma}\cdot\nabla w) - Rw, \tag{5}$$

where

$$K = \frac{(1-2\nu)\mu_f h_f^3 H}{12(1-\nu)(1-\nu_f)\eta}, \quad F = \frac{1-2\nu}{2(1-\nu)}\frac{Hh_f}{\eta}, \quad R = \frac{\mu_R}{\eta}. \tag{6}$$

As will be shown later, the wrinkling process is largely controlled by these three parameters plus the initial film stress.

III. SCALING ANALYSIS

In this section, we derive analytical solutions by a scaling analysis at the three stages of wrinkle evolution based on the model described in Sec. II. The results are summarized in Fig. 2, which schematically illustrates the three stages predicted for the evolution of wrinkle wavelength and amplitude.

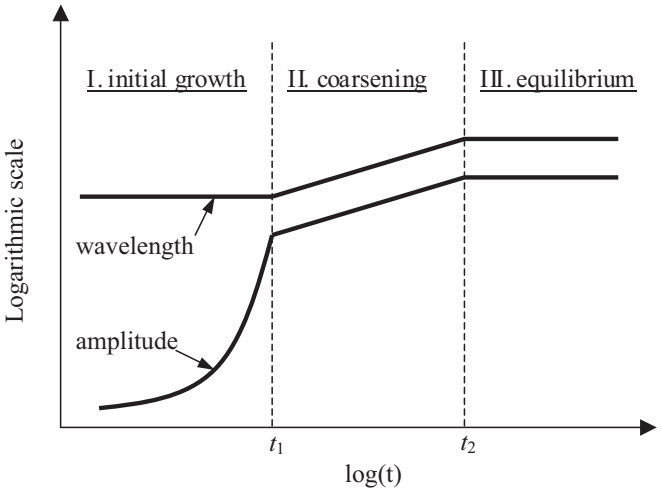

FIG. 2. Schematic illustration of the evolution of wrinkle wavelength and amplitude predicted by the scaling analysis. Stage I: initial growth, $\lambda\sim\lambda_m$, $A\sim\exp(t/4\tau_1)$; stage II: coarsening, $\lambda\sim(Kt)^{1/4}$, $A\sim(Kt)^{1/4}$; stage III: equilibrium, $\lambda\sim\lambda_{eq}$, $A\sim A_{eq}$. The predicted transition times, t_1 and t_2, are given by Eqs. (20) and (21), respectively.

A. Initial growth

At the early stage of wrinkling, the film stress is hardly relaxed. Consider an initial stress σ_0, where $\sigma_0<0$ for uniaxial or equibiaxial compression. The first two terms at the right-hand side of Eq. (5) compete to set a length scale

$$L_1 = \sqrt{-\frac{K}{F\sigma_0}} = \sqrt{-\frac{\mu_f h_f^2}{6(1-\nu_f)\sigma_0}}, \tag{7}$$

and a corresponding time scale

$$\tau_1 = \frac{K}{(F\sigma_0)^2} = \frac{(1-\nu)h_f\mu_f\eta}{3(1-2\nu)(1-\nu_f)H\sigma_0^2}. \tag{8}$$

Neglecting the third term at the right-hand side of Eq. (5) for the moment, a linear perturbation analysis [17] leads to a critical wavelength,

$$\lambda_c = 2\pi L_1, \tag{9}$$

and the fastest growing wavelength,

$$\lambda_m = 2\sqrt{2}\pi L_1, \tag{10}$$

both proportional to the length scale L_1, which in turn is proportional to the film thickness h_f. The film is unstable for wrinkles with wavelengths $\lambda>\lambda_c$, and the wrinkle amplitude grows exponentially with time at the initial stage. The growth rate, inversely proportional to the time scale τ_1, peaks at the wavelength $\lambda=\lambda_m$, for which the wrinkle amplitude is given by

$$A = A_0 \exp\left(\frac{t}{4\tau_1}\right). \tag{11}$$

Therefore, for the initial growth, the fastest growing mode dominates, with both the wrinkle wavelength and the growth rate depending on the film stress dictated by the relevant length and time scales.

The third term at the right-hand side of Eq. (5) accounts for the effect of substrate elasticity, which does not change the fastest growing wrinkle wavelength but reduces the growth rate. When the compressive film stress is lower than a critical stress, the substrate elasticity completely suppresses the wrinkling instability of the film. By setting the growth rate of the fastest growing wavelength to be zero, one obtains the critical stress

$$\sigma_c = -\sqrt{\frac{4KR}{F^2}} = -\sqrt{\frac{4(1-\nu)}{3(1-2\nu)(1-\nu_f)}\frac{h_f}{H}\mu_f\mu_R}. \tag{12}$$

Note that Eq. (12) predicts the critical stress under the assumption of thin viscoelastic layer (i.e., $H \ll \lambda_m$). The general solution for an arbitrarily thick viscoelastic layer can be found elsewhere [16].

B. Coarsening of wrinkles

As the wrinkle amplitude grows to be comparable to the film thickness, the film stress is significantly relaxed, and the nonlinear effect of the large deflection must be considered for the wrinkling process. It was found that, for a uniaxially compressed elastic film on a viscous substrate (i.e., $R=0$), there exists a kinetically constrained wrinkle state for each unstable wavelength [19]. In the neighborhood of such a state, the wrinkling process is very slow (i.e., $\partial w/\partial t \approx 0$) due to the viscous flow, despite the fact that the film remains energetically unstable. For a particular wavelength ($\lambda > \lambda_c$), setting $\partial w/\partial t = 0$ and $R=0$ in Eq. (5) leads to a spatially uniform stress in the film

$$\sigma_k = -\frac{4\pi^2 K}{\lambda^2 F} = -\frac{2\pi^2 h_f^2 \mu_f}{3(1-\nu_f)\lambda^2}. \tag{13}$$

Correspondingly, from Eqs. (3) and (4), the wrinkle amplitude is given by

$$A_k = h_f\sqrt{\frac{1}{3}\left(\frac{\lambda^2}{\lambda_c^2} - 1\right)}. \tag{14}$$

Therefore, the film stress can be continuously relaxed by increasing the wrinkle wavelength λ, i.e., coarsening. Meanwhile, the wrinkle amplitude grows.

Assume that the film stays in the neighborhood of the kinetically constrained states during coarsening, with both the wrinkle wavelength and the amplitude increasing. At this stage, the stress in the film is nearly uniform in the spatial distribution but relaxes over time, which is approximately given by Eq. (13) as a function of the wrinkle wavelength. In this case, comparing the first two terms in the right-hand side of Eq. (5) defines a time scale for coarsening:

$$\tau_2 = \frac{K}{(F\sigma_k)^2} = \frac{\lambda^4}{16\pi^4 K}. \tag{15}$$

Therefore, the wrinkle wavelength scales with the time as

$$\lambda \sim (Kt)^{1/4}. \tag{16}$$

The corresponding wrinkle amplitude can be obtained from Eq. (14). For $\lambda \gg \lambda_c$ (long time behavior), the same scaling law applies for the growth of wrinkle amplitude, i.e., $A \sim (Kt)^{1/4}$.

Notably, a molecular dynamics (MD) simulation of buckling molecular chains [20] showed a very similar scaling with both the wavelength and the amplitude growing as a power of time, $\lambda \sim t^n$, $w \sim t^\beta$, where both the exponents nearly equal to 0.26. MD simulations of compressed solid membrane [21] showed a coarsening dynamics with slightly larger exponents, $n=0.28$ and $\beta=0.29$. It has been noted that the nature of such dynamics is analogous to phase ordering phenomena such as spinodal decomposition [14,20,21].

C. Elastic equilibrium

For a viscoelastic layer with a rubbery limit, the substrate elasticity eventually stabilizes the wrinkle at an equilibrium state that minimizes the total strain energy in the film and the substrate [13,17]. Considering a uniaxially stressed film with a sinusoidal wrinkle of wavelength λ and setting $\partial w/\partial t = 0$ in Eq. (5), we obtain that

$$\sigma = -\frac{K}{F}\left(\frac{2\pi}{\lambda}\right)^2 - \frac{R}{F}\left(\frac{2\pi}{\lambda}\right)^{-2}. \tag{17}$$

Minimization of the stress gives an equilibrium wavelength

$$\lambda_{eq} = 2\pi\left(\frac{K}{R}\right)^{1/4} = 2\pi h_f\left[\frac{(1-2\nu)\mu_f H}{12(1-\nu)(1-\nu_f)\mu_R h_f}\right]^{1/4}. \tag{18}$$

The corresponding equilibrium wrinkle amplitude can be obtained from Eq. (3), namely

$$A_{eq} = h_f\sqrt{\frac{2}{3}\left(\frac{\sigma_0}{\sigma_c} - 1\right)}, \tag{19}$$

where σ_c is the critical stress given in Eq. (12). The same results were obtained by an energy minimization approach [13,17]. It is noted that, while the fastest growing wrinkle wavelength at the early stage depends on the initial stress in the film, the equilibrium wrinkle wavelength is independent of the stress. On the other hand, the equilibrium wrinkle amplitude increases with the magnitude of the stress.

A comparison between the fastest growing wavelength λ_m of the initial growth [Eq. (10)] and the equilibrium wavelength λ_{eq} [Eq. (18)] shows that when $|\sigma_0| > |\sigma_c|$, $\lambda_{eq} > \lambda_m$. Consequently, the intermediate stage is always coarsening, as sketched in Fig. 2. The transition points can be determined approximately using the scaling analysis. First, the coarsening starts when the initially fastest growing wrinkle ($\lambda = \lambda_m$) reaches the kinetically constrained state. From the exponential growth given in Eq. (11) and the wrinkle amplitude

given in Eq. (14), we obtain the first transition point

$$t_1 = 4\tau_1 \ln\left(\frac{h_f}{\sqrt{3}A_0}\right), \tag{20}$$

where A_0 is the initial amplitude at time $t=0$. Subsequently, following the power-law scaling in Eq. (16) for the wavelength coarsening, the second transition point is approximately given by

$$t_2 = t_1\left(\frac{\lambda_{eq}}{\lambda_m}\right)^4 = \frac{1}{R}\ln\left(\frac{h_f}{\sqrt{3}A_0}\right). \tag{21}$$

Therefore, the first transition time is proportional to the time scale of initial growth, which inversely scales with the square of the initial stress in the film, and the second transition time scales with the relaxation time $(1/R)$ of the viscoelastic layer, independent of the stress. Next we turn to numerical simulations and examine the predictions by the scaling analysis.

IV. NUMERICAL SIMULATION

Previously a finite difference method was used to simulate evolution of one-dimensional wrinkles [17]. In this paper, we adopt a spectral method to simulate wrinkling of two-dimensional films. For convenience the evolution equations are normalized by scaling lengths (coordinates and displacements), time, and stress components with h_f, η/μ_f, and μ_f, respectively. In addition, we split the linear and nonlinear terms so that the normalized evolution equations take the form

$$\frac{\partial w}{\partial t} = \frac{1-2\nu}{2(1-\nu)}\frac{H}{h_f}\left[-\frac{1}{6(1-\nu_f)}\nabla^2\nabla^2 w + \sigma^{(0)}_{\alpha\beta}\frac{\partial^2 w}{\partial x_\alpha \partial x_\beta} + \frac{\partial M_\beta}{\partial x_\beta}\right] - \frac{\mu_R}{\mu_f}w, \tag{22}$$

$$\frac{\partial u_\alpha}{\partial t} = \frac{H}{h_f}\frac{\partial}{\partial x_\beta}(\sigma^{(1)}_{\alpha\beta} + \sigma^{(2)}_{\alpha\beta}) - \frac{\mu_R}{\mu_f}u_\alpha, \tag{23}$$

where

$$\sigma^{(1)}_{\alpha\beta} = \frac{\partial u_\alpha}{\partial x_\beta} + \frac{\partial u_\beta}{\partial x_\alpha} + \frac{2\nu_f}{1-\nu_f}\frac{\partial u_\gamma}{\partial x_\gamma}\delta_{\alpha\beta}, \tag{24}$$

$$\sigma^{(2)}_{\alpha\beta} = \frac{\partial w}{\partial x_\alpha}\frac{\partial w}{\partial x_\beta} + \frac{\nu_f}{1-\nu_f}\frac{\partial w}{\partial x_\gamma}\frac{\partial w}{\partial x_\gamma}\delta_{\alpha\beta}, \tag{25}$$

$$M_\beta = (\sigma^{(1)}_{\alpha\beta} + \sigma^{(2)}_{\alpha\beta})\frac{\partial w}{\partial x_\alpha}. \tag{26}$$

Fourier transform of Eqs. (22) and (23) leads to

$$\frac{\partial \hat{w}}{\partial t} = \frac{1-2\nu}{2(1-\nu)}\frac{H}{h_f}\left[-\frac{1}{6(1-\nu_f)}k^4\hat{w} - \sigma^{(0)}_{\alpha\beta}k_\alpha k_\beta \hat{w} + ik_\beta \hat{M}_\beta\right] - \frac{\mu_R}{\mu_f}\hat{w}, \tag{27}$$

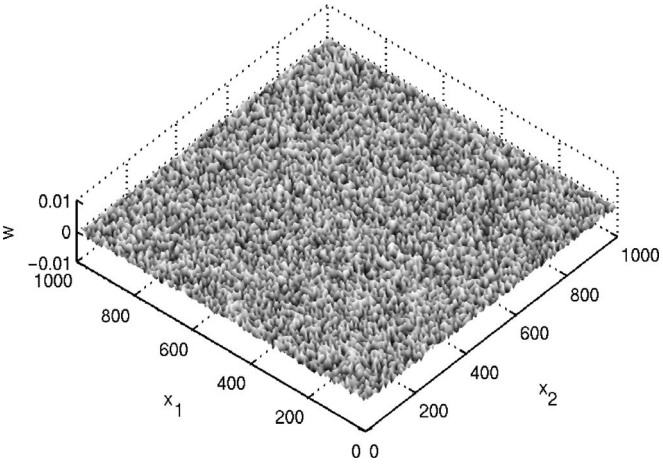

FIG. 3. A random perturbation of the lateral deflection as the initial condition for numerical simulations. Calculated RMS is 0.0006, and the average wavelength is 19.2.

$$\frac{\partial \hat{u}_\alpha}{\partial t} = \frac{H}{h_f}\left(-k^2\hat{u}_\alpha - \frac{1+\nu_f}{1-\nu_f}k_\alpha k_\beta \hat{u}_\beta + ik_\beta \hat{\sigma}^{(2)}_{\alpha\beta}\right) - \frac{\mu_R}{\mu_f}\hat{u}_\alpha, \tag{28}$$

where k_1 and k_2 are the components of the wave vector in the reciprocal Fourier space and $k=\sqrt{k_1^2+k_2^2}$.

A semi-implicit algorithm is employed to integrate Eqs. (27) and (28). First, the right-hand side of Eq. (27) consists of a linear part and a nonlinear part, namely

$$\frac{\partial \hat{w}}{\partial t} = B\hat{w} + \phi, \tag{29}$$

where

$$B = -\frac{1-2\nu}{2(1-\nu)}\frac{H}{h_f}\left(\frac{1}{6(1-\nu_f)}k^4 + \sigma^{(0)}_{\alpha\beta}k_\alpha k_\beta\right) - \frac{\mu_R}{\mu_f}, \tag{30}$$

$$\phi = \frac{1-2\nu}{2(1-\nu)}\frac{H}{h_f}ik_\beta \hat{M}_\beta. \tag{31}$$

Using a backward finite difference scheme for the linear part and a forward scheme for the nonlinear part, Eq. (29) is integrated point by point in the Fourier space as

$$\hat{w}^{(n+1)} = \frac{\hat{w}^{(n)} + \phi^{(n)}\Delta t}{1 - B\Delta t}, \tag{32}$$

where the superscript designates the time step and Δt is the time increment. The nonlinear term, $\hat{M}_\beta$, is obtained by Fourier transform of the quantity M_β; the latter is calculated in the real space using Eq. (26).

Similarly, for the in-plane displacements, we have

$$\frac{\partial \hat{u}_1}{\partial t} = C_1\hat{u}_1 + D_1\hat{u}_2 + \phi_1, \tag{33}$$

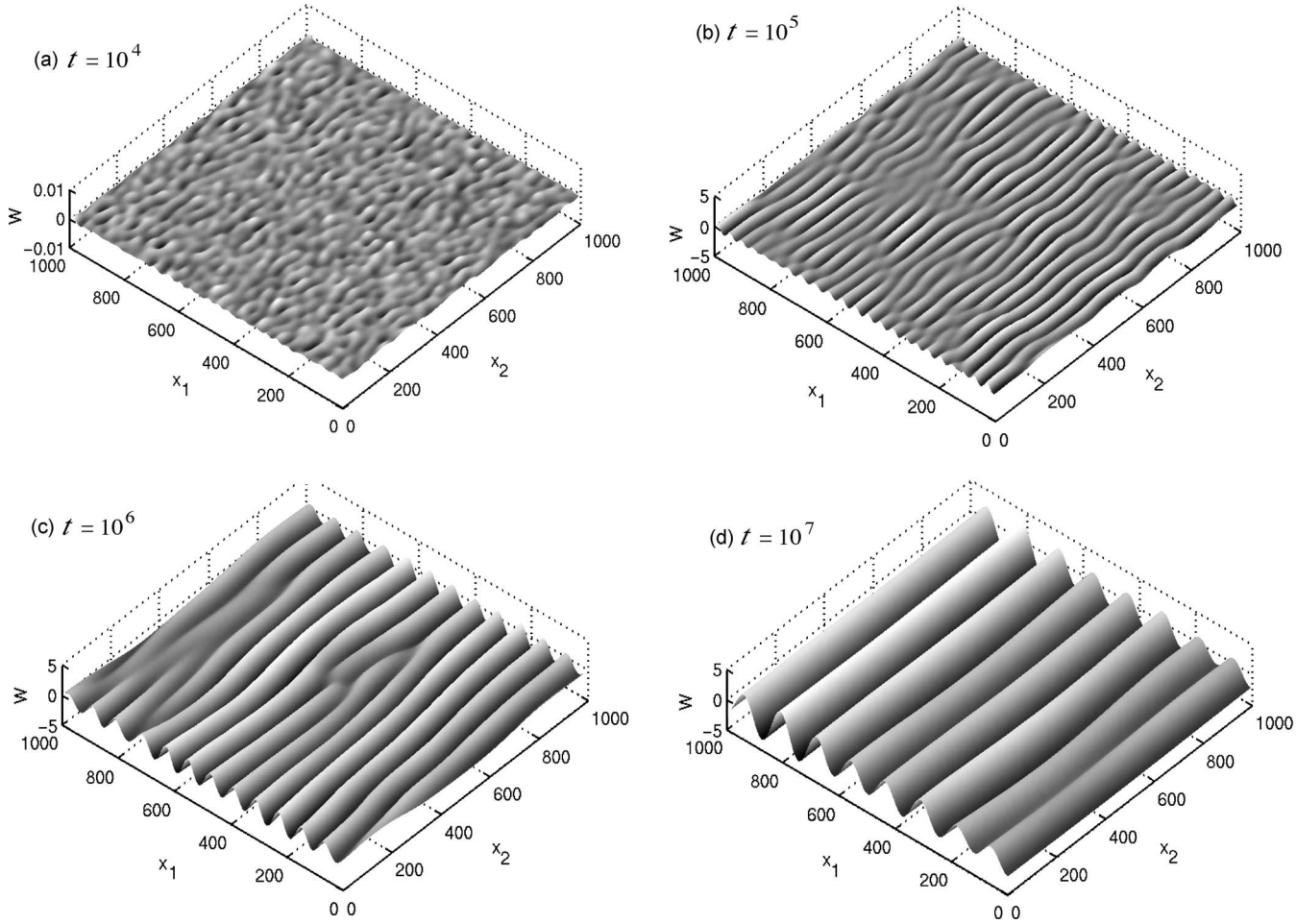

FIG. 4. A simulated evolution sequence of wrinkles in a uniaxially stressed film ($\sigma_{11}^{(0)}=-0.01$). (a) $\bar{\lambda}=46.2$ and $W_{\mathrm{RMS}}=0.00033$; (b) $\bar{\lambda}=44.4$ and $W_{\mathrm{RMS}}=0.313$; (c) $\bar{\lambda}=77.8$ and $W_{\mathrm{RMS}}=0.947$; (d) $\bar{\lambda}=128.2$ and $W_{\mathrm{RMS}}=1.66$.

$$\frac{\partial \hat{u}_2}{\partial t} = C_2\hat{u}_1 + D_2\hat{u}_2 + \phi_2, \tag{34}$$

where

$$C_1 = -\frac{H}{h_f}\left(\frac{2}{1-\nu_f}k_1^2 + k_2^2\right) - \frac{\mu_R}{\mu_f}, \tag{35}$$

$$C_2 = D_1 = -\frac{H}{h_f}\frac{1+\nu_f}{1-\nu_f}k_1k_2, \tag{36}$$

$$D_2 = -\frac{H}{h_f}\left(k_1^2 + \frac{2}{1-\nu_f}k_2^2\right) - \frac{\mu_R}{\mu_f}, \tag{37}$$

$$\phi_\alpha = \frac{H}{h_f}ik_\beta\hat{\sigma}_{\alpha\beta}^{(2)}. \tag{38}$$

Using the semi-implicit algorithm, Eqs. (33) and (34) are then integrated as

$$\hat{u}_1^{(n+1)} = \frac{(1-D_2\Delta t)(\hat{u}_1^{(n)} + \phi_1^{(n)}\Delta t) + D_1\Delta t(\hat{u}_2^{(n)} + \phi_2^{(n)}\Delta t)}{(1-C_1\Delta t)(1-D_2\Delta t) - C_2D_1(\Delta t)^2}, \tag{39}$$

$$\hat{u}_2^{(n+1)} = \frac{(1-C_1\Delta t)(\hat{u}_2^{(n)} + \phi_2^{(n)}\Delta t) + C_2\Delta t(\hat{u}_1^{(n)} + \phi_1^{(n)}\Delta t)}{(1-C_1\Delta t)(1-D_2\Delta t) - C_2D_1(\Delta t)^2}. \tag{40}$$

The numerical method in essence is the same as those used in Refs. [13,22], with the main difference being the treatment of the in-plane displacements. In both [13,22], the in-plane displacements were calculated using elastic equilibrium relations. Here they are calculated as evolving quantities in parallel with the lateral deflection. As discussed in [13], the spectral method resolves the challenges in numerical simulations by converting the high-order spatial differentiation in the real space into algebraic multiplication in the reciprocal Fourier space and utilizing the efficiency of fast Fourier transform (FFT) and its inverse to communicate between the two spaces. Similar numerical methods have been used for other evolution systems [23,24].

After normalization, physical parameters to be specified for simulations include the normalized initial stress $\sigma_{\alpha\beta}^{(0)}$, the modulus ratio μ_R/μ_f, the thickness ratio H/h_f, and Poisson's ratios ν and ν_f. The viscosity is absorbed into the normalized time. In this study, we consider two types of initial stresses: uniaxial ($\sigma_{11}^{(0)}=\sigma_0$, $\sigma_{22}^{(0)}=\sigma_{12}^{(0)}=0$) and equibiaxial ($\sigma_{11}^{(0)}=\sigma_{22}^{(0)}$

$=\sigma_0$, $\sigma_{12}^{(0)}=0$) with varying magnitudes. For the modulus ratio, we first consider a special case with $\mu_R/\mu_f=0$ to elucidate the dynamics of initial growth and coarsening, following which $\mu_R/\mu_f=10^{-5}$ is used to illustrate the effect of substrate elasticity. The other parameters are fixed for all simulations as, $H/h_f=10$, $\nu=0.45$, and $\nu_f=0.3$.

Numerically, a square computational cell in the x_1-x_2 plane with a periodic boundary condition is used. The size of the computational cell is selected such that it is sufficiently large compared to the longest wrinkle wavelengths (i.e., the equilibrium wavelength λ_{eq}), thus minimizing the effect of cell size on the simulation results. The cell is discretized into grids in both the x_1 and x_2 directions with a grid spacing small enough to resolve the shortest wavelength of interest (i.e., the critical wavelength λ_c). For the physical parameters considered in the present study, it has been determined that the cell size $L=1000h_f$ and a 128 by 128 grid are necessary and sufficient. The corresponding grid in the reciprocal space spans wave numbers from $-2\pi/15.6h_f$ to $2\pi/15.6h_f$ with a spacing $2\pi/1000h_f$. To start the simulation, a random perturbation of amplitude $0.001h_f$ is introduced to the lateral deflection of the initially flat film over the entire computational cell, as shown in Fig. 3. The semi-implicit algorithm for time integration is conditionally stable. To insure numerical stability and convergence, we use a time step $\Delta t=100$ (normalized by η/μ_f) for all simulations in the present study.

Quantitative characterization of complex wrinkle patterns is challenging [25]. In this study, two quantities are calculated to characterize the wrinkle patterns. First, the wrinkle amplitude is evaluated by a root-mean-square (RMS) of the lateral deflection, namely

$$W_{\mathrm{RMS}}(t)=\sqrt{\frac{\sum w(m,n,t)^2}{N^2}}, \tag{41}$$

where $w(m,n,t)$ is the deflection of the grid point (m,n) at time t and N is the number of grid points along one side of the cell (i.e., $N=128$ for the present study). As an example, for a one-dimensional sinusoidal wrinkle of amplitude A, $W_{\mathrm{RMS}}=A/\sqrt{2}$. Second, the average wrinkle wavelength is evaluated by

$$\bar{\lambda}(t)=\frac{2\pi}{\bar{k}(t)}, \tag{42}$$

where

$$\bar{k}(t)=\sqrt{\frac{\sum |\hat{w}(m,n,t)|^2 k(m,n)^2}{\sum |\hat{w}(m,n,t)|^2}}. \tag{43}$$

Equation (43) may be considered as a weighted RMS of the wave numbers, where the weight $|\hat{w}|^2$ represents the power intensity of the corresponding wave number, similar to the experimental plots of power spectra [14].

V. RESULTS AND DISCUSSIONS

A. Wrinkle growth and coarsening under uniaxial stresses

Figure 4 shows a sequence of simulated wrinkle patterns under a uniaxial stress with magnitude $\sigma_0=-0.01$ (normalized by the shear modulus μ_f). Here we set the modulus ratio $\mu_R/\mu_f=0$ and postpone discussions on the effect of substrate elasticity for a later section. Started with a random perturbation as shown in Fig. 3, a parallel stripe pattern emerges quickly in the direction perpendicular to the uniaxial stress. As the time advances, both the wrinkle amplitude and the wavelength increase [26]. Also can be seen is the presence of defects in the stripe patterns and the decrease of the defect density as the wrinkle evolves. Similar results are obtained for various stress magnitudes. Figure 5 plots the evolution of the average wrinkle wavelength and the RMS, both normalized by the film thickness h_f, and the time is normalized by η/μ_f. The average wavelength quickly reaches a plateau at a level depending on the initial stress [26]. This corresponds to

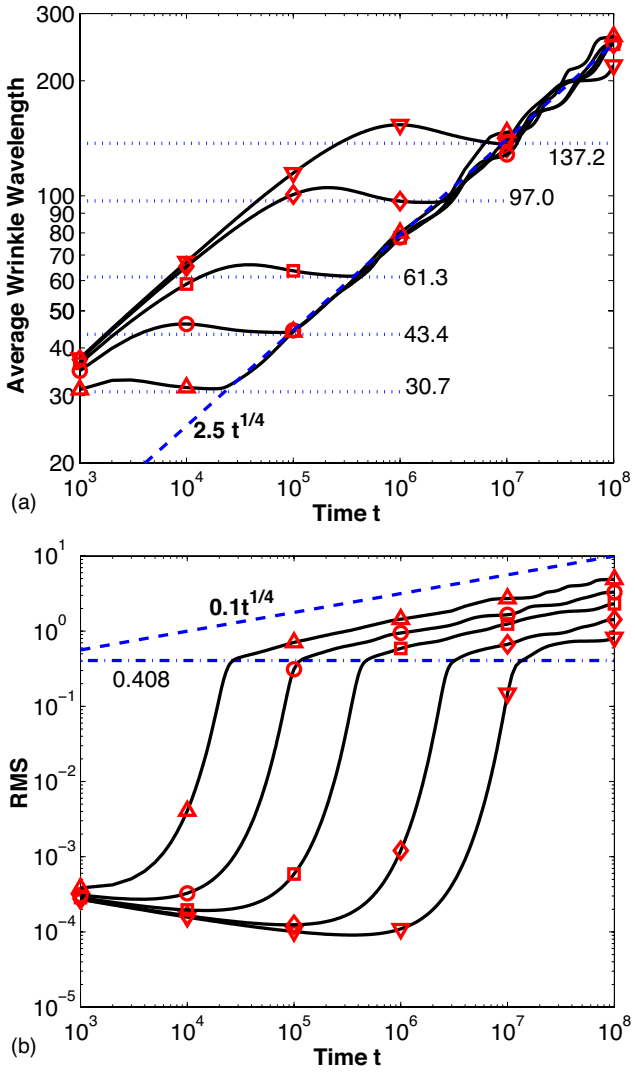

FIG. 5. (Color online) Evolution of wrinkle wavelength and RMS under uniaxial stresses: $\sigma_0=-0.02$ (△), -0.01 (○), -0.005 (□), -0.002 (◇), -0.001 (▽). The dotted lines in (a) indicate the fastest growing wavelengths predicted by the linear perturbation analysis. The dotted-dashed line in (b) corresponds to the stress-independent RMS at the kinetically constrained equilibrium states of the fastest growing wavelength. The dashed lines show the power-law scaling in both (a) and (b).

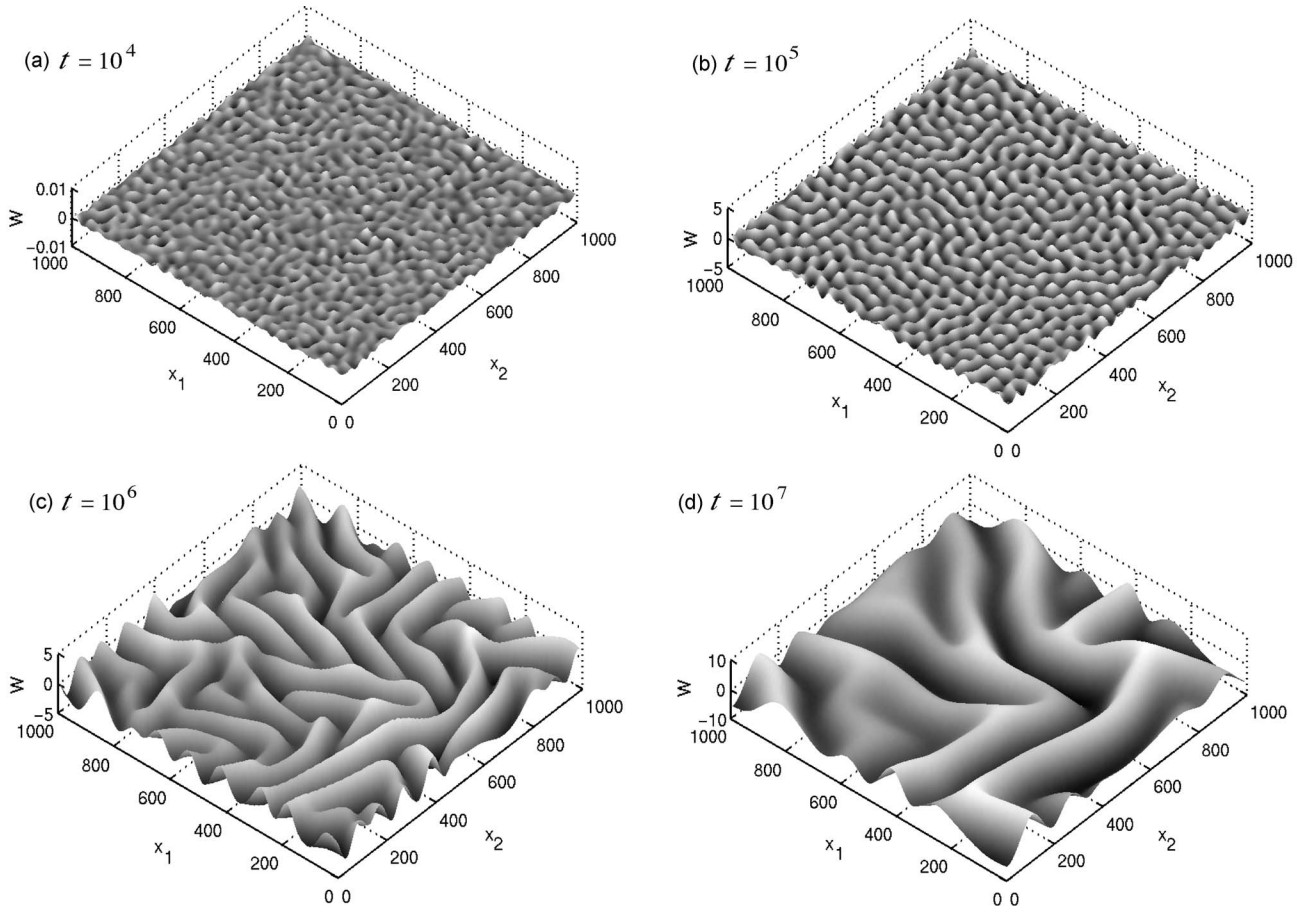

FIG. 6. A simulated evolution sequence of wrinkles in an equibiaxially stressed film ($\sigma_{11}^{(0)}=\sigma_{22}^{(0)}=-0.01$). (a) $\bar{\lambda}=42.8$ and $W_{\mathrm{RMS}}=0.00054$; (b) $\bar{\lambda}=45.1$ and $W_{\mathrm{RMS}}=0.423$; (c) $\bar{\lambda}=98.4$ and $W_{\mathrm{RMS}}=1.50$; (d) $\bar{\lambda}=196.9$ and $W_{\mathrm{RMS}}=3.18$.

the fastest growing mode predicted by Eq. (10) for the initial growth, as indicated in Fig. 5(a) by the horizontal dotted lines. At the same time, the RMS increases exponentially, as predicted by Eq. (11). The wavelength starts to increase (i.e., coarsening) when the RMS reaches a critical level ($\sim 0.3-0.4$), nearly independent of the initial stress. As indicated by the horizontal dashed line in Fig. 5(b), the RMS at the kinetically constrained state of wavelength $\lambda=\lambda_m$ is $1/\sqrt{6}=0.408$, which is close to the transition points for all stresses. Therefore, the first transition time predicted by Eq. (20) is a reasonable estimate of the onset of coarsening, which depends on the initial stress in the film.

During coarsening, the wavelength follows a straight line with a slope close to 1/4 in the log-log plot as shown in Fig. 5(a), in agreement with the power-law scaling predicted by the scaling analysis in Eq. (16). Remarkably, in spite of the different initial stresses and different transition points, the coarsening of the wrinkle wavelength follows essentially the same path. On the other hand, the wrinkle amplitude grows with the same scaling (after a short transition period) but with different magnitudes for different initial stresses, shown as parallel lines in Fig. 5(b). Since no elastic equilibrium state exists for the present case ($\mu_R/\mu_f=0$), the coarsening process continues until the simulation stops at $t=10^8$. Note that, to minimize the effect of computational cell size on the simulation results, the wrinkle wavelength should be limited to be small compared to the cell size. The longest wavelength in the present simulations is about one quarter of the cell size.

B. Wrinkle growth and coarsening under equi-biaxial stresses

Figure 6 shows a sequence of simulated wrinkle patterns under an equibiaxial stress of magnitude $\sigma_0=-0.01$, again with $\mu_R/\mu_f=0$. Differing from the stripe patterns under uniaxial stresses, a chaotic labyrinth pattern emerges. Figure 7 plots the evolution of the average wavelength and the RMS. Similar to the cases under uniaxial stresses, the average wavelength quickly reaches a plateau, corresponding to the same fastest growing wavelength predicted by the linear perturbation analysis, and the RMS increases exponentially during the initial growth. The transition point from initial growth to coarsening is about the same too, but the transition process is quite different. The coarsening of the wavelength is faster immediately after it reaches the transition point, giving a slope larger than 1/4 in the log-log plot [Fig. 7(a)]. The slope then decreases as coarsening continues, eventually approaching 1/4. Such a behavior may be attributed to the disorder of the labyrinth patterns. At the early stage of coarsening, the pattern is highly disordered with relatively short stripes in random directions, for which the dynamics are not well described by the scaling analysis assuming uniaxial

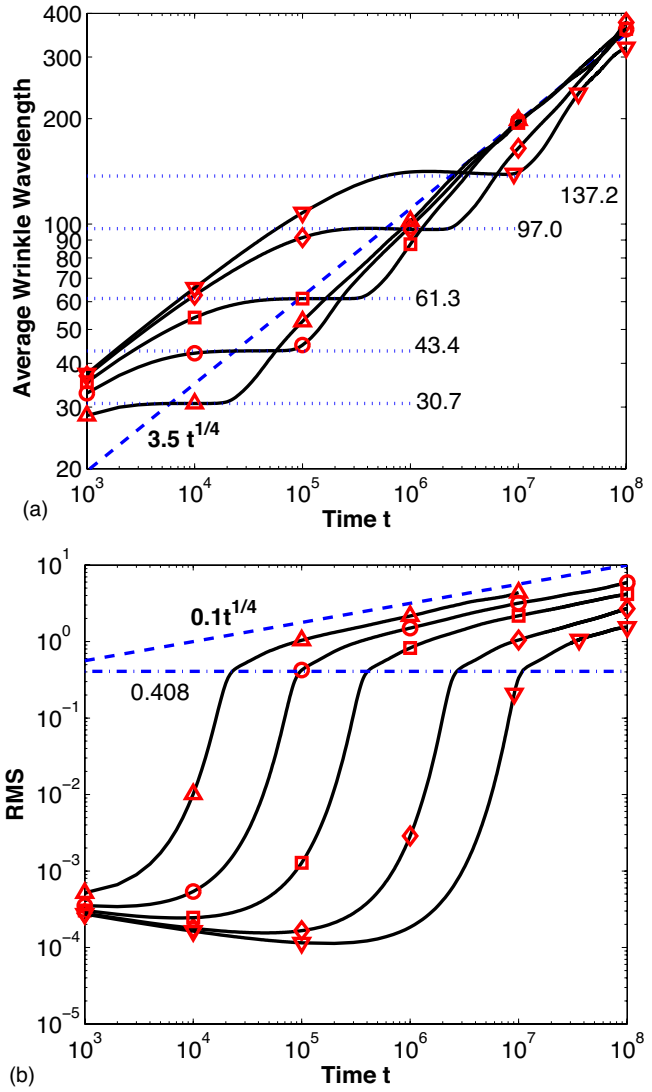

FIG. 7. (Color online) Evolution of wrinkle wavelength and RMS under equibiaxial stresses: $\sigma_0=-0.02$ (△), −0.01 (○), −0.005 (□), −0.002 (◇), −0.001 (∇). The dotted lines in (a) indicate the fastest growing wavelengths predicted by the linear perturbation analysis. The dotted-dashed line in (b) corresponds to the stress-independent RMS at the kinetically constrained equilibrium states of the fastest growing wavelength. The dashed lines show the power-law scaling in both (a) and (b).

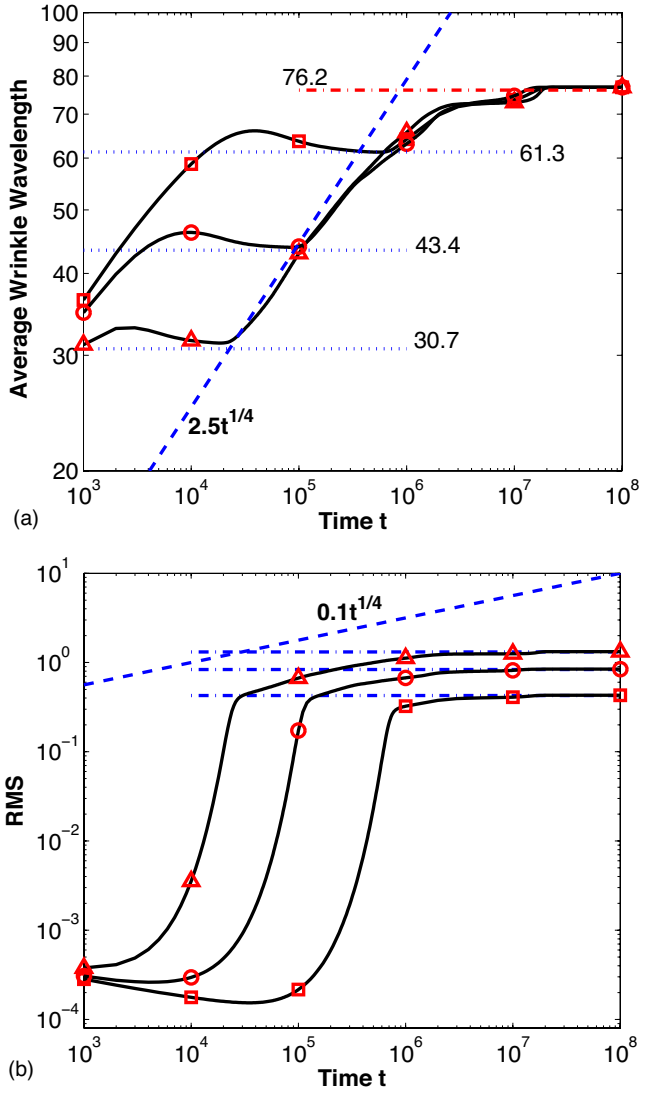

FIG. 8. (Color online) Evolution of wrinkle wavelength and RMS under uniaxial stresses: $\sigma_0=-0.02$ (△), −0.01 (○), −0.005 (□), with a modulus ratio $\mu_R/\mu_f=10^{-5}$. The dotted-dashed line in (a) indicates the equilibrium wrinkle wavelength, and the dotted-dashed lines in (b) indicate the equilibrium amplitudes.

stresses. Later on, while the pattern remains disordered, it consists of locally ordered long stripes coarsening in a similar manner as parallel stripes under uniaxial stresses. Consequently, the coarsening paths under equibiaxial stresses are different for different initial stress magnitudes, and they are different from those under uniaxial stresses. The growth of RMS under equibiaxial stresses is similar to that under uniaxial stresses, but with a longer transition period before it approaches the power-law scaling.

It should be pointed out that the present model does not account for the possible pinning of the elastic film at the bottom of the viscoelastic layer, as observed in some experiments after long-time annealing [14,15]. Thus, the maximum deflection is limited by the thickness of the viscoelastic layer (i.e., $H=10h_f$ for the present simulations). For $\sigma_0=-0.02$, the maximum deflection reaches this limit shortly after $t=10^7$, which stops the simulation.

C. Effect of substrate elasticity

The substrate elasticity has two major effects on the wrinkling process. First, it can stabilize the film under small stresses so that the film remains flat with no wrinkles at all. The critical stress is given by Eq. (12), for both uniaxial and biaxial stress states. The second effect is that, when the initial stress is high enough to cause wrinkling, the elastic limit of the substrate will eventually stabilize the wrinkle pattern. For parallel stripe patterns, the equilibrium wrinkle wavelength and amplitude are analytically given in Eqs. (18) and (19), respectively. For disordered stripes or labyrinth patterns

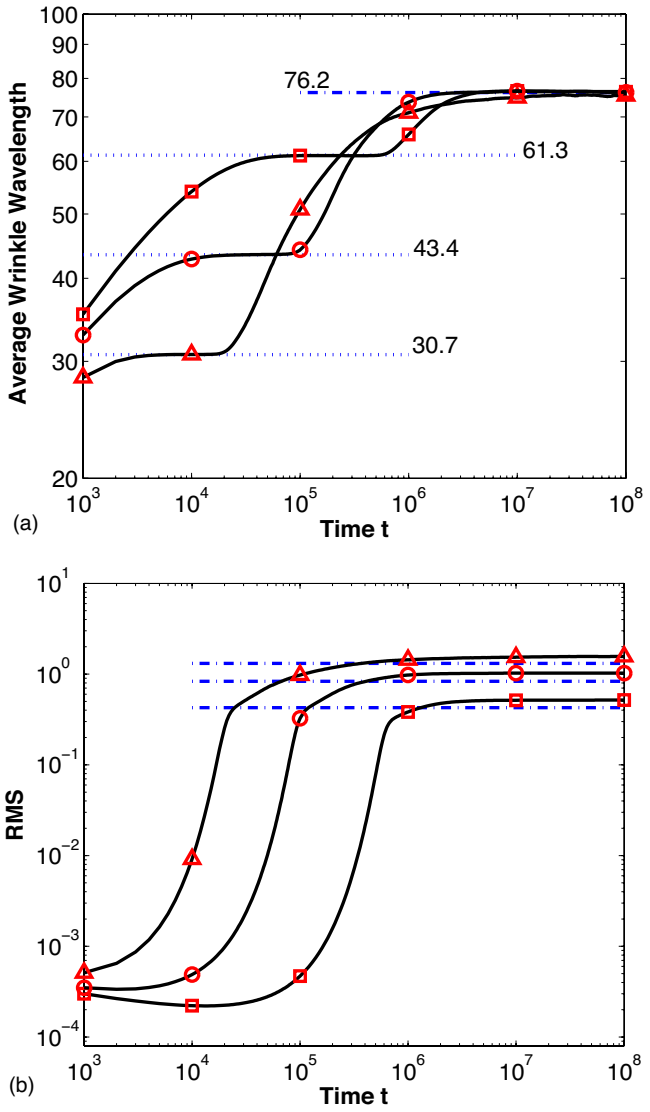

FIG. 9. (Color online) Evolution of wrinkle wavelength and RMS under equibiaxial stresses: $\sigma_0=-0.02$ (△), −0.01 (○), −0.005 (□), with a modulus ratio $\mu_R/\mu_f=10^{-5}$. The dotted-dashed line in (a) indicates the equilibrium wrinkle wavelength, and the dotted-dashed lines in (b) indicate the equilibrium amplitudes.

under equibiaxial stresses, however, no analytical solution is available for the equilibrium state.

Figure 8 plots the evolution of average wrinkle wavelength and RMS from numerical simulations under uniaxial stresses and with a rubbery modulus $\mu_R/\mu_f=10^{-5}$. The critical stress in this case is $\sigma_c=-0.00324$. When $|\sigma_0|<|\sigma_c|$, no wrinkle grows. For $|\sigma_0|>|\sigma_c|$, the initial growth is similar as in Fig. 5, but with a slower growth rate for the amplitude as predicted by the linear perturbation analysis [17]. The coarsening, however, is strongly influenced by the presence of the equilibrium state. The wavelength increases and eventually reaches another plateau, in agreement with the predicted equilibrium wavelength ($\lambda_e=76.2$ in this case) [27]. At the same time, the RMS approaches a plateau in agreement with the predicted equilibrium amplitude. The equilibrium wavelength is independent of the initial stress, while the equilibrium amplitude increases as the stress magnitude increases. Therefore, the power-law scaling for the coarsening dynamics becomes less predictive under the effect of substrate elasticity. In a special case, when $\sigma_0\approx\sigma_c$, the fastest growing wavelength is nearly the same as the equilibrium wavelength. Consequently, only one plateau would appear in the evolution of the wavelength, with no coarsening.

Figure 9 plots the evolution of wrinkle wavelength and RMS under equibiaxial stresses and with the same rubbery modulus, $\mu_R/\mu_f=10^{-5}$. Again, for $|\sigma_0|>|\sigma_c|$, the initial growth is well described by the linear perturbation analysis. The wavelength reaches a plateau during the initial growth, then coarsens, and eventually reaches the same equilibrium wavelength as for the uniaxial stresses. On the other hand, the RMS under an equibiaxial stress saturates at a plateau slightly higher than the equilibrium value under a uniaxial stress of the same magnitude, in agreement with a previous study [13].

For both uniaxial and equibiaxial stresses, as compared to Eq. (20), the transition from initial growth to coarsening is delayed by the substrate elasticity due to the reduced growth rate at the initial stage. The delay is more significant when the film stress is lower. For the second transition, the coarsening dynamics deviates from the power-law scaling long before it reaches the equilibrium. As a result, Eq. (21) significantly underestimates the time to reach equilibrium.

Figure 10 shows the wrinkle patterns for different stresses at the end of each simulation ($t=10^8$). Under uniaxial stresses [Fig. 10(a)], similar stripe patterns are obtained for different stress magnitudes, with the same wrinkle wavelength but different amplitudes. Under equibiaxial stresses [Figs. 10(b)–10(d)], although the average wavelength at equilibrium is independent of the initial stress, the coarsening dynamics leads to different evolution paths and thus different wrinkle patterns. It is found that, while the details of the wrinkle pattern stochastically depend on the initial perturbation, the average wavelength and the RMS capture the deterministic feature of the chaotic pattern.

D. Discussions on scaling

In Sec. III A, a length scale L_1 and a time scale τ_1 are obtained for the initial growth of wrinkles. Figure 11 replots the evolution of wrinkle wavelength from the numerical simulations [Figs. 5(a) and 7(a)], with no substrate elasticity), scaled by L_1 and τ_1. Remarkably, the evolution paths for different stress magnitudes collapse onto one for uniaxial stresses and another for equibiaxial stresses. At the early stage, the film selects the fastest growing wrinkle wavelength (i.e., the plateau in Fig. 11), which is the same for both uniaxial and equibiaxial stresses. Interestingly, the process of wavelength selection at the early stage seems to follow the same scaling as coarsening, i.e., $\lambda\sim t^{1/4}$. This process, however, strongly depends on the initial perturbation, and is typically too short to be captured in experiments. The difference between the two paths is in the dynamics of coarsening. Under uniaxial stresses, the coarsening process is well described by the power-law scaling with an exponent 1/4. Under equibiaxial stresses, however, it undergoes a transition stage

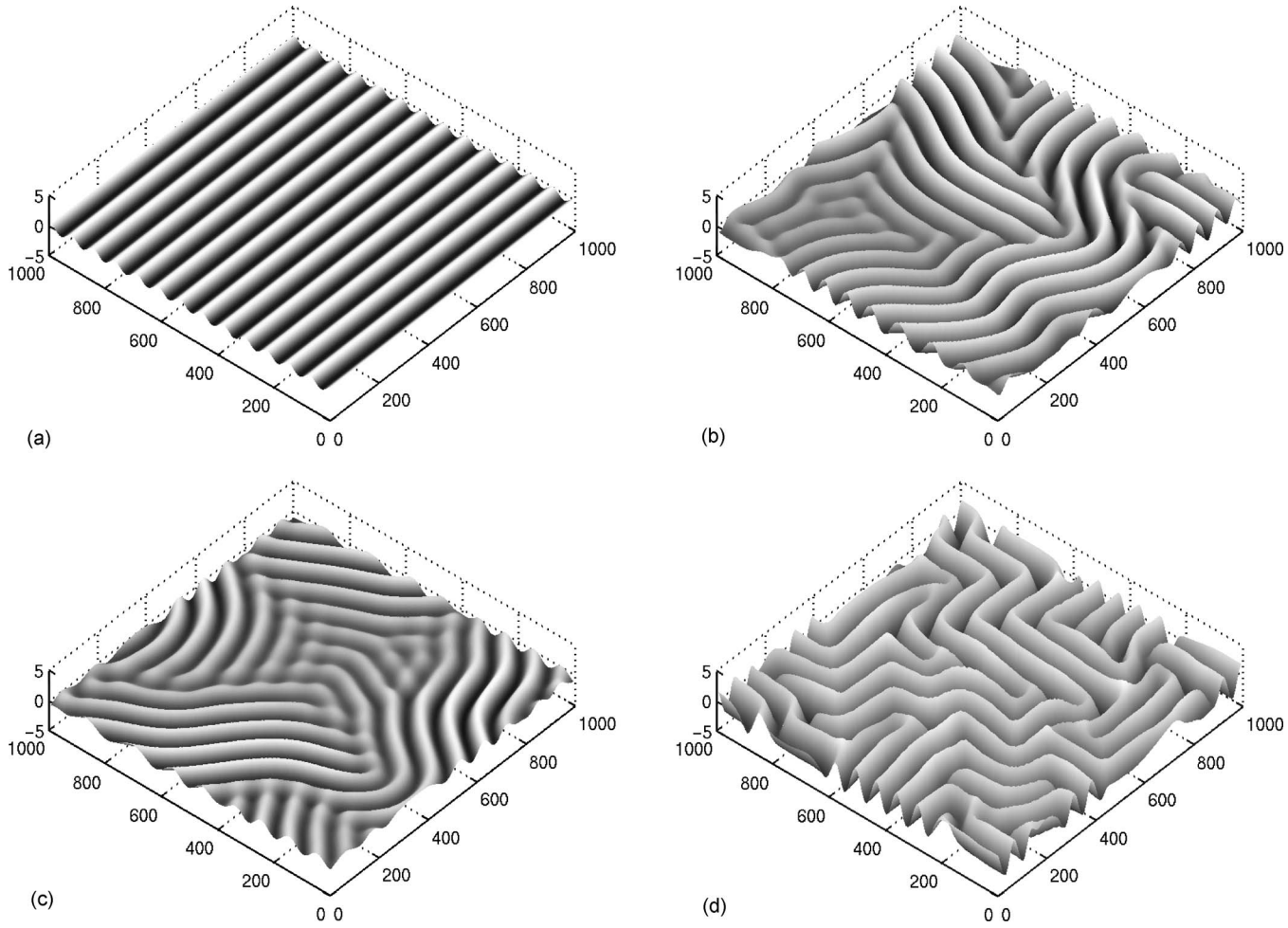

FIG. 10. Equilibrium wrinkle patterns with a modulus ratio $\mu_R/\mu_f=10^{-5}$: (a) under an uniaxial stress, $\sigma_0=-0.005$; (b) equibiaxial stress, $\sigma_0=-0.005$; (c) equibiaxial stress, $\sigma_0=-0.01$; (d) equibiaxial stress, $\sigma_0=-0.02$.

that starts with a faster coarsening rate. This is consistent with the MD simulations of buckling molecular chains [20] and membranes [21], with the chains under uniaxial stresses and the membranes under equibiaxial stresses. With substrate elasticity, however, the dynamics of coarsening is strongly influenced by the presence of the equilibrium state (Figs. 8 and 9), which does not follow the same scaling.

It should be noted that the above scaling analysis and numerical simulations are based on the model previously developed under the assumption that the thickness of the viscoleastic layer is small compared to the wrinkle wavelength ($H \ll \lambda$) and that the viscoelastic layer is compressible (i.e., $\nu < 0.5$). Following the same approach, different scaling can be derived for the cases with incompressible thin layers or thick substrates. For an incompressible thin layer ($\nu=0.5$), the evolution equation takes the form [17]

$$\frac{\partial w}{\partial t} = -K'\nabla^2\nabla^2\nabla^2 w + F'\nabla^2[\nabla\cdot(\boldsymbol{\sigma}\cdot\nabla w)] - Rw, \quad (44)$$

where

$$K' = \frac{\mu_f h_f^3 H^3}{18(1-\nu_f)\eta}, \quad F' = \frac{H^3 h_f}{3\eta}. \quad (45)$$

Comparing the first two terms in the right-hand side of Eq. (44) gives the same length scale as Eq. (7), but the time scale now becomes

$$\tau_1' = \frac{K'^2}{(F\sigma_0)^3} = \frac{h_f^3\mu_f^2\eta}{12(1-\nu_f)^2 H^3\sigma_0^3}. \quad (46)$$

At the kinetically constrained wrinkle states, the scaling, $\sigma_k \sim \lambda^{-2}$, still holds. Therefore, the coarsening of the wavelength now scales as $\lambda \sim t^{1/6}$. For a thick viscoelastic substrate ($H \gg \lambda$), it is more convenient to consider the Fourier transform of the evolution equation [13]. For the lateral deflection, the linearized evolution equation after Fourier transform takes the form

$$\frac{\partial \hat{w}}{\partial t} = \frac{1-\nu}{\eta k h_f}\left[-\frac{\mu_f k^4 h_f^4}{6(1-\nu_f)}\hat{w} - \sigma_0 k^2 h_f^2 \hat{w}\right] - \frac{\mu_R}{\mu_f}\hat{w}. \quad (47)$$

Again, the same length scale is obtained, but the time scale is

$$\tau_1'' = \frac{6(1-\nu_f)\eta}{(1-\nu)\mu_f}\left(\frac{L_1}{h_f}\right)^3 = \frac{\eta}{1-\nu}\sqrt{\frac{-\mu_f}{6(1-\nu_f)\sigma_0^3}}. \quad (48)$$

Therefore, the scaling for coarsening in this case is $\lambda \sim t^{1/3}$. It is speculated that, for a viscoelastic layer of an arbitrary

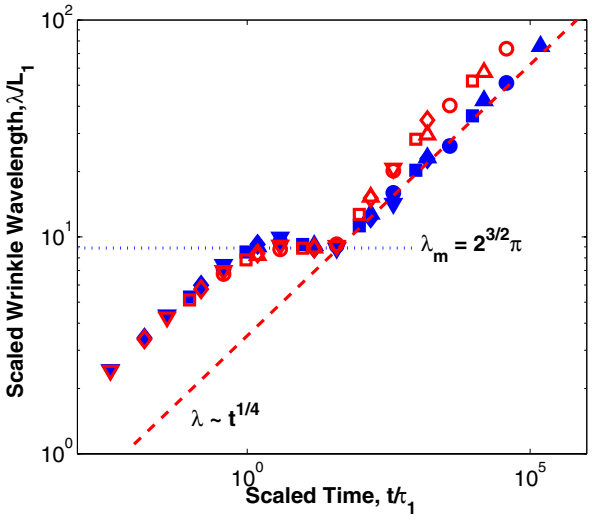

FIG. 11. (Color online) Evolution of wrinkle wavelength, scaled by the length L_1 and the time τ_1, under different uniaxial stresses (solid symbols) and equibiaxial stresses (open symbols).

thickness, the exponent of the power-law scaling for coarsening of wrinkles should be between 1/4 and 1/3 for a compressible layer and between 1/6 and 1/3 for an incompressible layer. A similar transition was noted for the phase separation kinetics of polymer blend films, where the coarsening exponent changes from 1 for thick films (100 nm) to a value near 0.5 for thin films (20 nm) [28]. While the power-law coarsening is analogous to other phase ordering phenomena as noted before [14,20,21], the dynamics of wrinkling is distinct and rich under the effects of stress and substrate elasticity.

Finally, we briefly comment on the comparison between the present modeling results and experimental observations. Qualitatively, the model reproduces most of the features observed in experiments (e.g., Ref. [14,15]), such as the wavelength of initial growth and subsequent coarsening as well as the equilibrium wrinkles in some cases. However, the coarsening exponent reported in [14] is close to 1, noticeably greater than the predicted exponents for either thin or thick viscoelastic layers. The cause of this discrepancy is unclear at this point. It may suggest that in experiments something other than the stress-driven, viscosity-controlled dynamics plays an important role. One suspect of such is the pinning of the top film at the surface of the rigid substrate supporting the thin viscoelastic layer, which was observed in some experiments [14,15]. However, it is questionable whether the pinning would increase the coarsening exponent as much as what was observed. More specific comparisons with experiments require the knowledge of elastic and/or viscoelastic properties of the materials and the stress in the film, which are often missing in the literature.

VI. SUMMARY

This paper presents a scaling analysis and two-dimensional numerical simulations of wrinkle growth and coarsening in stressed thin films on a viscoelastic layer. It is found that, during the initial growth, a stress-dependent wavelength is selected and the wrinkle amplitude grows exponentially over time. During coarsening, both the wrinkle wavelength and amplitude increases, following a power law with exponent 1/4 under uniaxial stresses. More complicated dynamics is predicted under equibiaxial stresses, which starts with a faster coarsening rate before approaching the same power-law exponent under uniaxial stresses. Furthermore, the coarsening dynamics is strongly influenced by the presence of an equilibrium state when substrate elasticity is included. The equilibrium wrinkle patterns under uniaxial and equibiaxial stresses have the same wavelength, but the wrinkle amplitude is slightly higher under equibiaxial stresses for the same stress magnitude.

Similar power-law scaling is derived for a stressed elastic film on an incompressible thin viscoelastic layer or on a thick viscoelastic substrate. The analogy between the wrinkling dynamics and other phase ordering phenomena is noted, and comparison between the modeling results and experimental observations is discussed.

ACKNOWLEDGMENTS

The authors are grateful for the support by the National Science Foundation through Grant CMS-0547409, and by DARPA through the University of Texas AP2C (Grant No. HR0011-06-1-0005).

[1] N. Bowden, S. Brittain, A. G. Evans, J. W. Hutchinson, and G. M. Whitesides, Nature (London) **393**, 146 (1998).
[2] E. Cerda and L. Mahadevan, Phys. Rev. Lett. **90**, 074302 (2003).
[3] F. Iacopi, S. H. Brongersma, and K. Maex, Appl. Phys. Lett. **82**, 1380 (2003).
[4] H. Yin, R. Huang, K. D. Hobart, J. Liang, Z. Suo, S. R. Shieh, T. S. Duffy, F. J. Kub, and J. C. Sturm, J. Appl. Phys. **94**, 6875 (2003).
[5] M. Watanabe, H. Shirai, and T. Hirai, J. Appl. Phys. **92**, 4631 (2002).
[6] S. P. Lacour, S. Wagner, Z. Y. Huang, and Z. Suo, Appl. Phys. Lett. **82**, 2404 (2003).
[7] C. Harrison, C. M. Stafford, W. Zhang, and A. Karim, Appl. Phys. Lett. **85**, 4016 (2004).
[8] J. R. Serrano and D. G. Cahill, J. Appl. Phys. **92**, 7606 (2002).
[9] K. Efimenko, M. Rackaitis, E. Manias, A. Vaziri, L. Mahadevan, and J. Genzer, Nat. Mater. **4**, 293 (2005).
[10] H. G. Allen, *Analysis and Design of Structural Sandwich Panels* (Pergamon, New York, 1969).
[11] J. Groenewold, Physica A **298**, 32 (2001).
[12] X. Chen and J. W. Hutchinson, J. Appl. Mech. **72**, 597 (2004).

[13] Z. Y. Huang, W. Hong, and Z. Suo, J. Mech. Phys. Solids **53**, 2101 (2005).
[14] P. J. Yoo and H. H. Lee, Phys. Rev. Lett. **91**, 154502 (2003).
[15] P. J. Yoo and H. H. Lee, Macromolecules **38**, 2820 (2005).
[16] R. Huang, J. Mech. Phys. Solids **53**, 63 (2005).
[17] S. H. Im and R. Huang, J. Appl. Mech. **72**, 955 (2005).
[18] L. D. Landau and E. M. Lifshitz, *Theory of Elasticity* (Pergamon, London, 1959).
[19] R. Huang and Z. Suo, J. Appl. Phys. **91**, 1135 (2002).
[20] L. Golubovic, D. Moldovan, and A. Peredera, Phys. Rev. Lett. **81**, 3387 (1998).
[21] D. Moldovan and L. Golubovic, Phys. Rev. Lett. **82**, 2884 (1999).
[22] Z. Y. Huang, W. Hong, and Z. Suo, Phys. Rev. E **70**, 030601(R) (2004).
[23] W. Lu and Z. Suo, J. Mech. Phys. Solids **49**, 1937 (2001).
[24] A. A. Golovin, S. H. Davis, and P. W. Voorhees, Phys. Rev. E **68**, 056203 (2003).
[25] D. A. Egolf, I. V. Melnikov, and E. Bodenschatz, Phys. Rev. Lett. **80**, 3228 (1998).
[26] A slight overshooting is observed in Figs. 4 and 5 for the initial growth under uniaxial stresses. This may be understood as a fluctuation in the process of selecting the fastest growing wavelength from the initially random perturbation. No overshooting is observed in Fig. 7 under equibiaxial stresses, which indicates a somewhat different selection process at the early stage. Such a difference can be related to the landscapes of the growth rate with respect to the wave vector. Under a uniaxial stress, the growth rate peaks at two points corresponding to the wave number (positive and negative) of the fastest growing mode in the direction of the uniaxial stress. Under an equibiaxial stress, the growth rate peaks on a circular ring with the wave number as its radius, with no directional preference.
[27] There appears to be another plateau before the wrinkle wavelength reaches the equilibrium plateau in Fig. 8(a). In the present simulations, with a computational cell of size $L = 1000h_f$ and under the periodic boundary condition, the equilibrium plateau corresponds to the wrinkle wavelength that minimizes the total elastic energy in the system, which consists of 13 wrinkle waves in the direction of uniaxial stress [see Fig. 10(a)]. The additional plateau corresponds to the state with 14 wrinkle waves, the next to minimum energy state within the computational cell. The finite size of the computational cell leads to discrete energy states for periodic wrinkles. The random initial perturbation introduces sufficient defects that facilitate relatively smooth coarsening far away from equilibrium. Near equilibrium, the defect density is low and the coarsening from 14 waves to 13 waves becomes more difficult and takes a longer time.
[28] L. Sung, A. Karim, J. F. Douglas, and C. C. Han, Phys. Rev. Lett. **76**, 4368 (1996).